

Broadband spectroscopy of astrophysical ice analogues

IV. Optical constants of N₂ ice in the terahertz and mid-infrared ranges

F. Kruczkievicz^{1,2*}, A.A. Gavdush³, F. Ribeiro^{1,6}, D. Campisi^{4,5**}, A. Vyjidak¹, B.M. Giuliano¹, G.A. Komandin³, S.V. Garnov³, T. Grassi¹, P. Theulé², K.I. Zaytsev³, A.V. Ivlev¹, and P. Caselli¹

¹ Max-Planck-Institut für Extraterrestrische Physik, Gießenbachstraße 1, Garching, 85748, Germany

² Aix Marseille Univ, CNRS, CNES, LAM, Marseille, France

³ Prokhorov General Physics Institute of the Russian Academy of Sciences, 119991 Moscow, Russia

⁴ Institute for Theoretical Chemistry, University of Stuttgart, Pfaffenwaldring 55, Stuttgart, Germany

⁵ Department of Engineering, University of Perugia, Via Duranti 93, 06125 Perugia, Italy

⁶ Federal Institute of Education, Science and Technology of Rio de Janeiro (IFRJ), Nilópolis Campus - Rio de Janeiro - Brazil

Received 2024; accepted 2024

ABSTRACT

Context. Understanding the optical properties of astrophysical ices is crucial for modeling dust continuum emission and radiative transfer in dense, cold interstellar environments. Molecular nitrogen, a primary carrier of N in protoplanetary disks, plays a key role in the formation of nitrogen-bearing species. However, the lack of direct measurements of the terahertz (THz)–infrared (IR) optical constants of N₂ ice introduces uncertainties in radiative transfer models, snowline locations, and disk mass estimates.

Aims. We present direct measurements and analysis of the optical properties of N₂ ice across a broad THz–IR spectral range by combining THz pulsed spectroscopy (TPS) and Fourier-transform IR spectroscopy (FTIR). The observed optically active THz vibrational modes of N₂ ice are supported by density functional theory (DFT) calculations. The consistency of our measurements and calculations with data sets from the literature is also assessed.

Methods. N₂ ice was grown at cryogenic temperatures via the gas-phase deposition onto a cold silicon window. The optical properties of the ice samples were quantified using our earlier-reported method: it involves the direct reconstruction of the THz complex refractive index from the TPS data, combined with the derivation of IR response from the FTIR data using the Kramers-Kronig relations. The N₂ ice response was parameterized using the Lorentz model of complex dielectric permittivity, which was verified with our DFT calculations and compared with the literature data.

Results. The complex refractive index of N₂ ice is quantified in the frequency range of $\nu = 0.3\text{--}16$ THz (the wavelength range of $\lambda = 1\text{ mm}\text{--}18.75\text{ }\mu\text{m}$), and compared with the DFT results as well as with the available literature data. The observed resonant absorption peaks at $\nu_L = 1.47$ and 2.13 THz, with the damping constants of $\gamma_L = 0.03$ and 0.22 THz, respectively, are attributed to the well-known optically active phonons of the α -N₂ crystal.

Conclusions. We provide a complete set of the THz–IR optical constants for N₂ ice by combining TPS and FTIR spectroscopy. Our results have implications for future observational and modeling studies of protoplanetary disk evolution and planet formation.

Key words. astrochemistry – methods: laboratory: solid state – ISM: molecules – techniques: spectroscopic – Infrared: ISM

1. Introduction

The distribution and abundance of ice components in protoplanetary disks are crucial for shaping the properties of emerging planetary systems. Ices influence both the growth and the inward migration of dust grains – the fundamental building blocks of planets, while also dictating the reservoir of key volatile elements (Gundlach & Blum 2015; Drążkowska & Alibert 2017; Sturm et al. 2023). The ice composition plays an important role in the thermodynamics and mass transfer in a disk, thus affecting the snowlines’ location and the efficiency of planetesimal formation (Öberg et al. 2011; Arabhavi et al. 2022; Gavino et al.

2023). Measurements and analysis of dust and ice opacities are powerful tools for better constraining the physical and chemical properties of disks. While the underlying optical constants are known, observations of dust continuum emission and self-consistent modeling of dust opacity provide refined estimates of the disk mass, composition, and snowlines, as compared to those coming from models based on the bare-grain assumption (Arabhavi et al. 2022). The key to realizing these improvements is obtaining reliable optical constants of ices across a wide terahertz (THz)–infrared (IR) range relevant to protoplanetary disks.

Traditionally, ice optical constants have been derived using the Fourier-transform IR (FTIR) spectroscopy, which yields only the amplitude transmission spectra and which is commonly aided by the Kramers-Kronig relations to retrieve the phase for the complete characterization of an ice sample (Bergren et al. 1978; Hagen & Tielens 1981; Hudgins et al. 1993). Although this approach has led to invaluable catalogs of optical data, reliance on the underlying assumptions and mathematical derivations can introduce measurement uncertainties. To mitigate this

* Present address: Leiden Observatory, Leiden University, Niels Bohrweg 2, 2333 CA Leiden, The Netherlands

** Present address: Aarhus Institute of Advanced Studies (AIAS), Aarhus University, Høegh-Guldbergs Gade 6B, 8000 Aarhus C, Denmark; Center for Interstellar Catalysis, Department of Physics and Astronomy, Aarhus University, 1520-337 Ny Munkegade 120, 8000 Aarhus C, Denmark

difficulty, the THz pulsed spectroscopy (TPS) technique was applied by [Giuliano et al. \(2019\)](#) to measure the THz response of ices with no need for the Kramers-Kronig transform. Indeed, TPS offers a favorable opportunity to detect the THz waveform transmitted through an analyte, the Fourier transform, which gives spectral amplitude and phase. This makes it possible to directly retrieve the THz complex refractive index in a broad spectral range. It was shown by [Gavdush et al. \(2022\)](#) that the spectral phase of TPS can be used to calibrate that of FTIR data, and thus to eliminate the Kramers-Kronig transform uncertainty, facilitating the broadband characterization of laboratory ices. Such a technique was then applied to comprehensively analyze the THz-IR optical constants of CO and CO₂ ices ([Gavdush et al. 2022](#)), as well as their scattering properties and porosity ([Gavdush et al. 2025](#)) relying on the broadband optical spectra.

The next goal of our broadband spectroscopic measurements is the characterization of N₂ ice. Among all volatiles, molecular nitrogen is recognized as a primary nitrogen carrier in the protoplanetary disks. It plays a crucial role in the formation of abundant N-bearing gas phase species such as NH₃ and N₂H⁺ (e.g. [Hily-Blant et al. 2010](#)). In our Solar System, the presence of N₂ ice has been confirmed in dwarf planets Pluto and Eris and Neptune's largest moon Triton ([Tegler et al. 2010, 2012](#)).

Because N₂ has no strong dipole moment, it is notoriously difficult to observe directly, as it lacks strong optically active vibrational modes. Estimates of its abundance depend on the indirect tracers, such as N₂H⁺, the CN/HCN ratio, and various nitriles ([Qi et al. 2019; van 't Hoff et al. 2017](#)). These proxies provide valuable constraints on the N₂ distribution, especially in cold outer disks, where N₂ is expected to freeze out once temperatures drop below 20–25 K ([Minissale et al. 2022](#)). However, indirect methods inevitably introduce observational and chemical modeling uncertainties, highlighting the need for complementary approaches, particularly in the solid phase. Understanding the ice reservoir of N₂ is important not only to constrain its overall abundance but also to elucidate its role in the formation of species bearing N on grains in the densest disk regions ([Walsh et al. 2014](#)).

In this study, N₂ ice is grown at cryogenic temperatures and measured using TPS and FTIR techniques. The optical properties of N₂ ice are retrieved in a broad spectral range spanning the frequencies of $\nu = 0.3\text{--}16$ THz, or the wavelengths of $\lambda \approx 1\text{ mm--}18.75\text{ }\mu\text{m}$. The observed optically active vibrational modes are attributed to the quadrupole moments of a molecule in a crystalline lattice, parametrized by the Lorentz model, and supported by density functional theory (DFT) calculations and available literature data. The obtained data on the THz-IR optical properties of N₂ ice would be useful for modeling nitrogen freeze-out and chemistry in protoplanetary disks. Our findings can be used to calculate how the opacities of dust grains change when they are covered in ice mantles, particularly in spectroscopic regions where the ices' resonance features are present. This information aids in the interpretation of dust continuum emission, including variations expected between dense and diffuse regions where the fraction of ice-coated grains differs.

2. Methods

2.1. The experimental setup

The experimental studies were conducted at the CASICE laboratory developed at the Center for Astrochemical Studies at the Max Planck Institute for Extraterrestrial Physics (Garching, Germany). Data obtained with the TPS ([Giuliano et al. 2019](#)) and

FTIR ([Müller et al. 2018](#)) spectrometers were combined to derive the broadband optical constants of N₂ ice.

In the original design of our laboratory, the same vacuum chamber can be coupled to both the TPS and the FTIR spectrometers. A motorised translation stage moves the chamber between the sample compartments of the two spectrometers and adjusts the position relative to the beam. This ensures that the ice samples analyzed with the two instruments have reproducible properties for given deposition conditions. Therefore, the spectroscopic data recorded in the THz and IR ranges can be directly merged for the calculation of the broadband complex refractive index of an ice. However, the measurements have not been performed on an identical set of ice samples.

A scheme of the vacuum chamber, TPS and FTIR arrangements are detailed in [Gavdush et al. \(2022\)](#). The 15 cm diameter vacuum chamber is equipped with a high-power closed-cycle cryocooler (Advanced Research Systems), which cools down the sample holder to a temperature of 5 K in normal operation mode. To provide homogeneous ice deposition (over the optical aperture of a substrate) for the experiments, in this work, the radiation shield was removed from the sample holder, reaching a minimum achievable temperature of 11 K. A base pressure of $\approx 10^{-7}$ mbar is set when the system is cold via a pumping station composed of a turbomolecular pump combined with a backing rotary pump.

The substrate is placed in the middle of the vacuum chamber and the optical windows of the chamber are made of the high-resistivity float-zone silicon (HRFZ-Si) with the high refractive index of $n_{\text{Si}} \approx 3.4$, negligible dispersion, and small absorption in the desired THz-IR range. It is worth noting that the broadband dielectric response of this THz-IR optical material is almost independent of temperature.

The TPS spectrometer (BATOP TDS-1008) features a broad spectral range of 0.05–3.5 THz, with a maximum at ≈ 1.0 THz and a spectral resolution as high as ≈ 0.03 THz. In this TPS system, a pair of photoconductive antennas are pumped and probed by a femtosecond fiber laser (TOPTICA), serving as an emitter and a detector of THz pulses. A customized sample compartment allocates the cryocooler, while the TPS housing is kept under cold nitrogen gas purging, aimed at suppressing an impact of atmospheric water along the beam path on the measured THz data.

A Bruker IFS 125HR FTIR spectrometer is used to record the transmission IR spectra of ice, with a resolution as high as $\approx 1\text{ cm}^{-1}$ (≈ 0.03 THz). A Mylar Multilayer beam splitter, an FIR-Hg source and an FIR-DTGS detector were selected to work in the FIR and mid-IR ranges. A customized flange accommodates the cryocooler in the spectrometer sample compartment, which is kept under vacuum.

2.2. The experimental protocol

The ice samples for the TPS and FTIR measurements were grown under the same experimental conditions. Following the experimental procedure by [Giuliano et al. \(2019\)](#), the ice layers are formed by the condensation from the gas phase through a 6-mm-diameter stainless steel pipe placed at ≈ 7 cm from the substrate to ensure uniform deposition on both sides. A metering valve regulated the N₂ flux. To minimize H₂O and CO₂ contamination in the gas flow entering the vacuum chamber, the last part of the gas line includes a trap, made of a copper coil and immersed in liquid nitrogen. Such a trap reduces the total gas flux and, thus, increases by ≈ 3 times the required deposition time

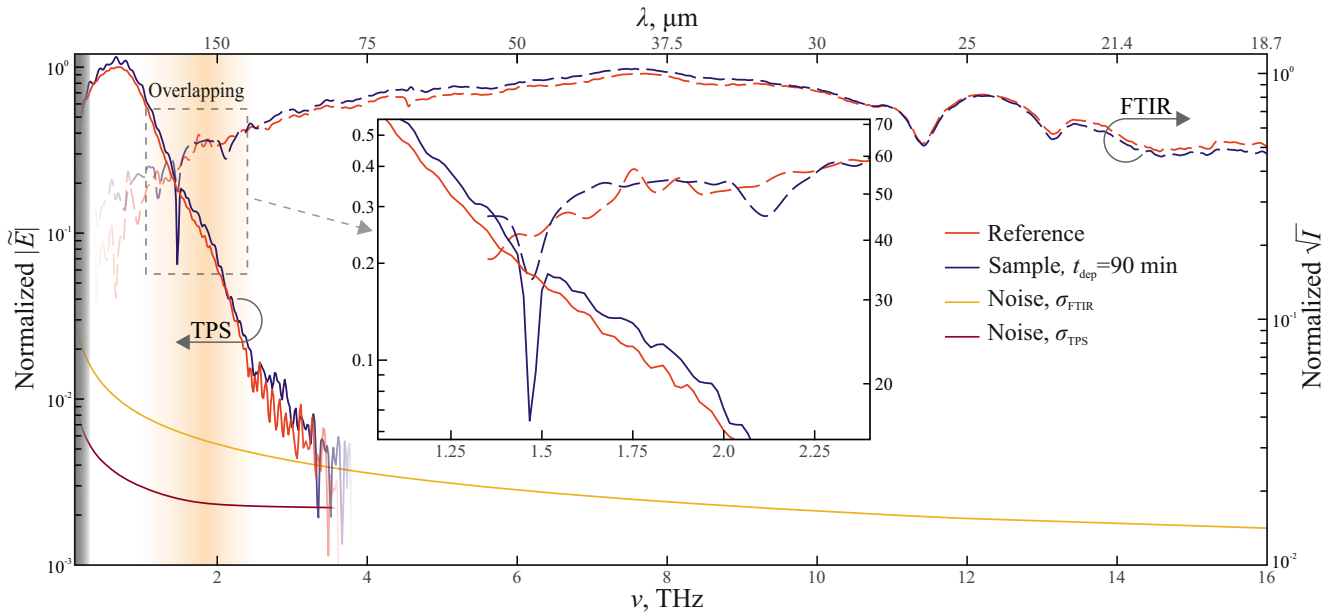


Fig. 1. Reference and sample spectra of N₂ ice, measured by the TPS (solid lines) and FTIR (dashed lines) spectrometers at specified deposition steps, t_{dep} , and normalized by the maximum of the corresponding reference spectrum (for convenience). The low-frequency gray-shaded area shows the spectral range where distortions are expected owing to the THz beam diffraction at the sample aperture (Giuliano et al. 2019). The orange-shaded area near ≈ 2.0 THz (enlarged in the inset for clarity) indicates where the TPS and FTIR data overlaps. Sensitivity of the TPS and FTIR measurements is characterized by the standard deviation of the corresponding instrumental noise, σ_{TPS} and σ_{FTIR} as described by Gavdush et al. (2022).

to reach the same ice thickness as reported in our earlier studies (Giuliano et al. 2019; Gavdush et al. 2022; Gavdush et al. 2025).

A thickness on the order of a fraction of a millimeter is required to obtain a reliable reconstruction of the THz–IR optical constants, so the chosen deposition rate must be fast enough to grow thick ice in a reasonable experimental time. To achieve this condition, the pressure was maintained at $\approx 10^{-4}$ mbar, while each deposition step was set to 9 min, minimizing heating of the HRFZ-Si substrate due to gas condensation. The total deposition time was 90 min, resulting in an overall ice thickness of approximately 1.72 mm. The ice layers on the front and back sides of the substrate reached thicknesses of about 1.028 mm and 0.689 mm, respectively. The substrate temperature was maintained at 11 K prior to deposition and increased slightly to 12 K during each deposition cycle. Between consecutive steps, the system was allowed to equilibrate until the substrate temperature returned to 11 K.

2.3. TPS and FTIR data processing

For both the TPS and FTIR measurements, reference spectra of the bare substrate were recorded before the start of the deposition process. The sample signals were measured every second deposition step after 18 min. The Tukey (Tukey et al. 1986) and 4th-order Blackman-Harris (Harris 1978) apodization windows were applied for pre-processing of the TPS waveforms and FTIR interferograms, respectively. For the TPS data, the application of the Fourier transform results in the frequency-domain complex amplitude $\tilde{E}(\nu)$, with both the amplitude and phase information, which makes possible the direct reconstruction of the THz complex dielectric permittivity of an analyte (Giuliano et al. 2019). In turn, FTIR gives the power spectrum $I(\nu) \propto |\tilde{E}(\nu)|^2$ with only the amplitude information (Griffiths & de Haseth 1986).

From the reference (bare substrate) and sample measurements we define the experimental transmission coefficients of

the ice films. For TPS, where the complex electric-field spectrum $\tilde{E}(\nu)$ is available, the complex transmission amplitude reads

$$\tilde{T}_{\text{exp,TPS}}(\nu) = \frac{\tilde{E}_{\text{sample}}(\nu)}{\tilde{E}_{\text{reference}}(\nu)}, \quad (1)$$

whereas for FTIR, which provides intensities, we report the amplitude of the transmission as

$$|\tilde{T}_{\text{exp,FTIR}}(\nu)| = \sqrt{\frac{I_{\text{sample}}(\nu)}{I_{\text{reference}}(\nu)}}. \quad (2)$$

These definitions link the complex transmission of Fig. 2 to the E - and I -spectra in Fig. 1. In the next step, the TPS and FTIR datasets are merged by (i) reconstructing the FTIR phase via the Kramers–Kronig transform and (ii) matching amplitudes and phases to the TPS reference, following the procedure detailed in Gavdush et al. (2022).

In Fig. 1, the reference and sample spectra are acquired by TPS and FTIR systems for the N₂-ice samples of different thicknesses. The shaded spectral range of the TPS and FTIR data overlapping near ≈ 2.0 THz is broad enough to make merging the spectral data possible. We have no absorption lines except at 1.5 and 2.13 THz. For both the TPS and FTIR systems, in Fig. 1, the spectral noise levels are estimated in the form of frequency-dependent standard deviations $\sigma_{\text{TPS}}(\nu)$ and $\sigma_{\text{FTIR}}(\nu)$, to highlight the variability of the reference spectra as detailed by Gavdush et al. (2022). Fig. 2 (a),(b) illustrates the merging of the TPS and FTIR data for the N₂ ice after a 54-min-long deposition. In the overlapping range, the measured TPS (green markers) and FTIR (blue markers) data are close. The weighted superposition of the transmission spectra in the overlapping range is used to calculate the broadband transmission amplitude $|\tilde{T}(\nu)|$, while the spectral signal-to-noise ratios of our spectrometers ensure a

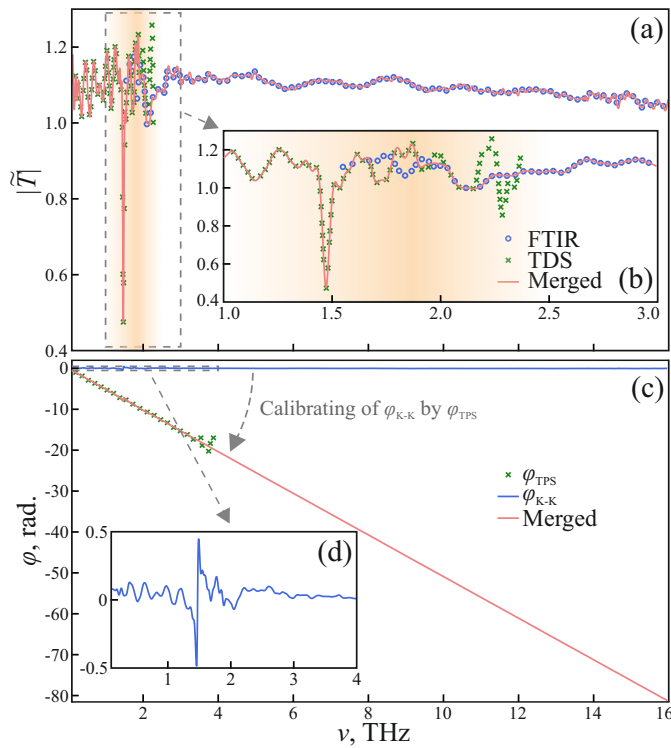


Fig. 2. Merging of the TPS and FTIR data for N₂ ice after the 54-min-long deposition. (a) Amplitude of the complex transmission coefficient $|\tilde{T}(\nu)|$ retrieved from the TPS (green markers) and FTIR (blue) data, and the resultant merged curve (red) see Eqs. (1)–(2) for the definitions of the transmission coefficients. (b) Zoom-in on the TPS and FTIR overlapping data. (c) Phase of the complex transmission coefficient $\phi(\nu)$, where the TPS phase ϕ_{TPS} (green markers), FTIR-based Kramers-Kronig phase $\phi_{\text{K-K}}$ (blue line), and resultant broadband phase (red) are shown. (d) Low-frequency behavior of the FTIR-based Kramers-Kronig phase $\phi_{\text{K-K}}$.

smooth transition from the lower to higher frequencies as shown by Gavdush et al. (2022). In Fig. 2 (c), the missing IR phase is retrieved from the FTIR data using the Kramers-Kronig transform (Martin 1967; Lucas et al. 2012), while a knowledge of the low-frequency TPS phase allows for mitigating the Kramers-Kronig transform uncertainty (Gavdush et al. 2022).

In this way broadband complex transmission spectra $\tilde{T}(\nu)$ was obtained from the experiments and used to retrieve both the thicknesses of N₂ ice samples and their complex refractive index $\tilde{n} = n - i\alpha c_0 / (2\pi\nu) \equiv \sqrt{\tilde{\epsilon}}$ in the frequency range of 0.3–16.0 THz, where n is a real refractive index, α is an absorption coefficient (by field)¹, $c_0 = 3 \times 10^8$ m/sec is the speed of light in vacuum, while $\tilde{\epsilon} = \epsilon' - ie''$ is the complex dielectric permittivity. For this, we use the earlier-reported approach (Giuliano et al. 2019; Gavdush et al. 2022) that minimizes the error functional – i.e., a discrepancy between the experimental complex transmission spectrum $\tilde{T}(\nu)$ and its theoretical model, which accounts for all key features of the radiation–sample interactions: reflections at interfaces, absorption and phase delay in bulk, standing waves in layers, finite coherence length, and signal apodization. Moreover, determining the position of satellite pulses from the TPS waveforms is used to find the thicknesses of the ice layers (Giuliano et al. 2019).

¹ We note that the power absorption coefficient (within the radiative transfer theory) is given by $\mu_\alpha = 2\alpha$.

2.4. Theoretical analysis

2.4.1. Analytical model of complex dielectric permittivity

Resonant absorption peaks observed in the broadband dielectric spectra of the N₂ ice were modeled by a superposition of the Lorentz kernels

$$\tilde{\epsilon}(\nu) = \epsilon_\infty + \sum_{j=1}^2 \frac{\Delta\epsilon_j \nu_{\text{L},j}^2}{\nu_{\text{L},j}^2 - \nu^2 + i\nu\gamma_{\text{L},j}}, \quad (3)$$

where $\Delta\epsilon_j$, $\nu_{\text{L},j}$, and $\gamma_{\text{L},j}$ are the amplitude, resonant frequency, and damping constant of the j^{th} Lorentz term, while ϵ_∞ is the constant dielectric permittivity at higher frequencies. Parameters $\nu_{\text{L},j}$ and $\gamma_{\text{L},j}$ indicate the spectral position and width of each Lorentz oscillator, while $\Delta\epsilon_j$ is responsible for its contribution to the total dielectric response. It is worth noting that this model is physically-rigorous since it satisfies the sum rule (Martin 1967; Komandin et al. 2022) and the Kramers-Kronig relations (Martin 1967; Lucas et al. 2012). This favorably distinguishes the model defined by Eq. (3) from a series of Gaussian bands often used to analyse the astrophysical ice absorption properties (Boogert et al. 2015).

The first approximations for the model parameters are estimated from the reconstructed dielectric response, including positions and width of the absorption peak, where the magnitude of the peak can be estimated from the real dielectric permittivity. Owing to the convenience of presenting results via $n(\nu)$ and $\alpha(\nu)$, this form was chosen for the measured data representation; if needed, this can be easily converted to ϵ' and ϵ'' , as detailed above.

2.4.2. DFT calculations of vibrational modes

To simulate the far-IR spectra, the α -phase of the N₂ crystal was considered, as expected in our experimental conditions (Wyckoff 1963). It features the primitive cubic crystalline lattice, characterized by four molecules per unit cell of the volume of 179.79 Å³ and the period of 5.64 Å. Such a unit cell was repeated $2 \times 2 \times 2$ times, and the gas-phase cluster model was created by removing the N atoms at the boundaries. This allows us to model solid materials with high accuracy by using gas-phase codes, enabling the use of a higher-level theory.

To compute the IR spectra in the THz region (see Appendix A), we employed DFT implemented in the ORCA code (Neese et al. 2020). We used the B3LYP exchange-correlation functional (Becke 1993; Lee et al. 1988) and a triple-zeta valence basis set with polarization functions Def2-TVZP (Weigend & Ahlrichs 2005). This method has been reported to reproduce experimental spectra in the THz region of solid-state species belonging to the 2p series of the periodic table (Cutini & Ugliengo 2021; Kambara 2014; Wang & Wang 2012; Chen et al. 2004; Oppenheim et al. 2010; Dash et al. 2015). Dispersion correction was not taken into account (see Appendix A), as it causes a redshift of the vibrational modes.

Vibrational frequencies were computed using the harmonic approximation. We opted not to optimize the experimental structure (Wyckoff 1963), because the optimization leads to the larger interatomic distances and, thus, to significant changes in the absorption peak positions. The self-consistent field convergence was achieved when the relative energy change is lower than 10^{-14} . The resolution of identity (RI-JONX method) (Neese 2003) approximation was applied to reduce the computational cost for the Coulomb integral only, but not for the Hartree-Fock

exchange, in order to ensure the highest possible accuracy at a lower computational cost, using an auto-generated auxiliary basis set (Stoychev et al. 2017) by ORCA.

3. Results

In Fig. 3, the estimated broadband dielectric response of N_2 ice deposited at 11 K is shown as the refractive index n and absorption coefficient α by field. Yellow curve and green-shaded areas stand for the average values and $\pm 1.5\sigma$ (or 87%) confidence intervals, calculated from the ensemble of measurements at the different deposition times in the 18–90 min range with the 18 min step. As shown by Gavdush et al. (2022), the sensitivity of our spectrometers significantly impacts the reconstruction accuracy, especially in the case of a low-absorbing species. Therefore, in Fig. 3 (c), approximations for the detection limit are calculated from the TPS and FTIR noises (σ_{TPS} and σ_{FTIR} , shown in Fig. 1) as a function of the deposition time t_{dep} (or the total sample thickness l) as detailed in (Gavdush et al. 2022). From these estimates, one notices that two absorption peaks at lower frequencies are above the detection limit, while all the IR background absorption is below. Thus, we further analyze only these two physically-reasonable absorption peaks while neglecting the background that is more likely attributed to noise.

In Fig. 3, the complex dielectric permittivity model defined by Eq. (3) is estimated and overlapped with the experimental curves, while the resultant model parameters are summarized in Table 1. The absorption peaks observed at 1.47 and 2.13 THz agree with the literature data on studies of the solid-state nitrogen – i.e., the molecular crystal, the THz–IR response of which depends on the crystalline structure (Ron & Schnepp 1967; Anderson & Leroi 1966a; Louis & Schnepp 1969; Scott 1976; Savchenko et al. 2019).

As discussed in Sec. 2.4.2, the applied growth conditions presume that the N_2 ice is in the α phase. In such a case, the factor group analysis predicts 24 normal modes for the $\text{Pa}3$ space group, among which only three are translational phonon modes T_u , including the single acoustic and two optically active T_u phonons. These modes were analyzed theoretically and studied experimentally via the FTIR and neutron scattering techniques by several groups; for example, see (Ron & Schnepp 1967; Anderson & Leroi 1966a; Louis & Schnepp 1969; Kjems & Dolling 1975). The two optical features and the associated absorption bands show some variations between different experiments. For instance, by comparing our results with those of Ron & Schnepp (1967), we obtain a $\approx 30\%$ discrepancy for the ratio of the amplitude absorption values (0.35 in Ron & Schnepp (1967) versus 0.27 in the present study) and the ratio of the integrated absorption intensities (0.76 in Ron & Schnepp (1967) versus 1.11 in our work).

Broadening and some asymmetry of the 2.13 THz peak (as compared to the Lorentz model) might indicate anharmonicity effects, which can be explained by the dependence between the mode frequency and damping (Hardy & Karo 1982), or the morphological features of ice (porosity, disorder, and polycrystallinity). A somewhat monotonic increase in the N_2 -ice absorption at higher frequencies (> 8.0 THz) is attributed to the scattering on heterogeneities of an analyte (such as pores, as reported by Gavdush et al. (2025)). This effect indirectly evidences the imperfect ice structure but is still below the defined detection limit.

Our DFT calculations of the α - N_2 vibrational modes depict two harmonic frequencies, representing the expected translational movements of N_2 molecules and pointed out in Fig. 3.

From Table 2, we also notice that these vibrational modes agree with both our and earlier-reported experiments, as well as the theoretical predictions based on the interatomic potentials (Zunger & Huler 1975). The discrepancies are quite small – at the level of a few inverse centimeters. They are in close agreement within the DFT accuracy (Banks et al. 2020). Our theoretical analysis not only reproduced the α - N_2 translational modes, but also revealed some temperature dependence of the lattice structure and the resultant evolution of vibrational modes with temperature (see Appendix A). However, this aspect is beyond the scope of this article. Thereby, both the literature survey on the response of solid nitrogen and the DFT simulations justify the origin of the N_2 -ice vibrational modes observed in our THz–IR spectroscopic experiments.

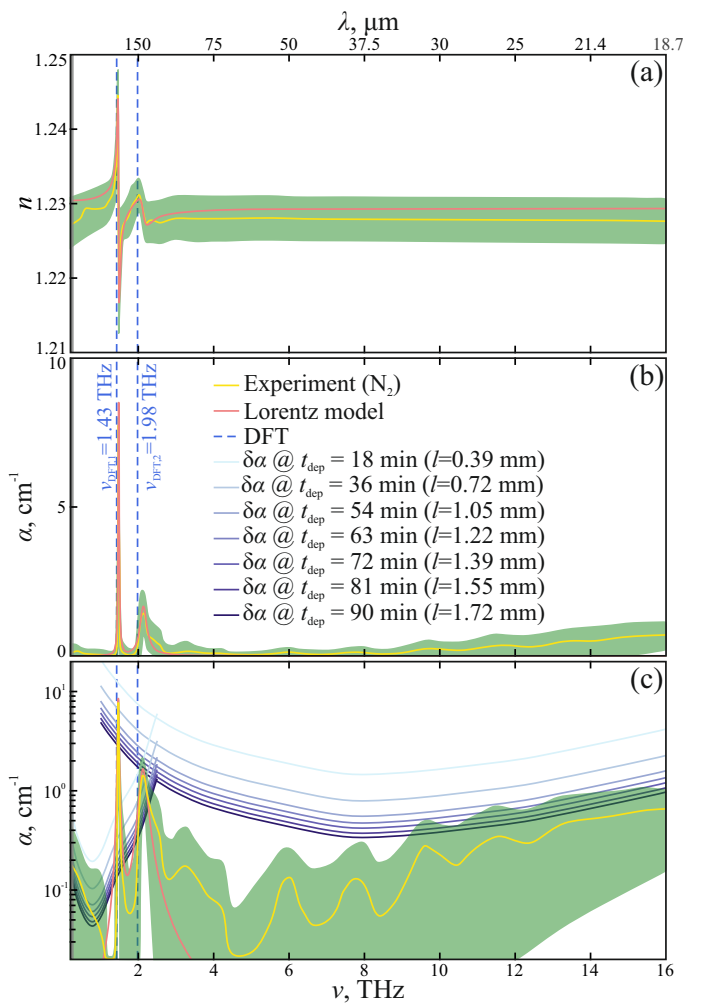


Fig. 3. Broadband THz–IR optical properties of the N_2 ice, deduced from the measurements of sample of different thicknesses l . The yellow solid lines show the mean values, the green shaded zones, the $\pm 1.5\sigma$ (87%) confidence intervals of the measurements, while the red solid lines, the complex dielectric permittivity model defined by Eq. 3 and Table 1. (a) Refractive index n . (b, c) Absorption coefficient α (by field) in the linear and logarithmic scales, respectively. In (c), the blue-shaded solid lines define the 3σ detection limits for the absorption $\delta\alpha$, calculated for the different ice thicknesses l (measured with the ~ 0.01 mm uncertainty). In (a)–(c), the vertical blue dashed lines define the frequencies of the α - N_2 vibrational modes predicted by the DFT method.

Table 1. Parameters of the complex dielectric permittivity model of N₂ ice defined by Eq. (3), with $\pm 1\sigma$ confidence intervals.

Parameter	Value
ϵ_∞	1.51 ± 0.01
$\Delta\epsilon_1$	$(16 \pm 1) \times 10^{-4}$
$\nu_{L,1}$, THz	1.47 ± 0.01
$\gamma_{L,1}$, THz	0.03 ± 0.01
$\Delta\epsilon_2$	$(9.6 \pm 2.2) \times 10^{-4}$
$\nu_{L,2}$, THz	2.13 ± 0.02
$\gamma_{L,2}$, THz	0.22 ± 0.03

4. Discussion and conclusions

In this work, we combined TPS and FTIR spectroscopy to study the THz–IR response of laboratory analogs of N₂ astrophysical ice. The main results of our findings can be summarized as:

1. The optical properties of N₂ ice deposited on the HRFZ-Si substrate at the temperature of 11 K were retrieved in the 0.3–16 THz frequency range or the 1 mm–18.75 μ m wavelength range. Two resonant absorption peaks of N₂ ice, those above the detectable absorption level of our spectrometers, were observed at the frequencies of 1.47 and 2.13 THz (204 and 141 μ m) and attributed to the optically active translational phonon modes of the α -N₂ molecular crystal. The 2.1 THz peak exhibits broadening and asymmetry, possibly due to anharmonicity effects or morphological features, such as porosity and polycrystallinity. A monotonic increase in absorption at higher frequencies (> 8 THz), although below the detection limit, is attributed to the scattering on the ice heterogeneities and, thus, also highlights the imperfections in its structure.
2. The complex dielectric permittivity of N₂ ice was modeled by a pair of the Lorentz kernels, which reproduce the observed vibrational modes and have the resonant frequencies of $\nu_L = 1.47$ and 2.13 THz and the damping constants of $\gamma_L = 0.03$ and 0.22 THz, respectively. The observed resonances were compared with the DFT prediction and the available literature data on the phonon spectrum of α -N₂ molecular crystal. This made it possible to justify the correctness of our experimental findings and theoretical interpretations.
3. The density functional theory has predicted the translational modes of α -N₂ within 5 cm⁻¹ compared to our findings. We have found that translational modes are sensitive to the geometrical structure of α -N₂. Small variations in the interatomic distances, which are temperature-dependent, can drastically change the far-infrared spectra.
4. Our optical constants for N₂ ice cover the far-infrared and submillimeter range, which is poorly sampled by current space-based observatories. While JWST provides high-sensitivity coverage in the near- to mid-infrared, and ALMA operates at longer (submillimeter) wavelengths, a spectral gap remains in the far-infrared (30–200 μ m). Our data help fill this gap from the modeling side. Future instruments such as PRIMA (Probe far-InfraRed Mission for Astrophysics), currently in development, are expected to provide observational access to this range with high spectral resolution and sensitivity. In this context, the dielectric response of solid N₂ obtained in this study provides valuable input for radiative transfer models of N₂-rich environments, such as the outer regions of protoplanetary disks.

Finally, accurate optical constants across a broad spectral range are essential for modeling dust and ice in protoplanetary disks. Misestimates of the refractive index can lead to errors in radiative transfer calculations, affecting the inferred disk temperature, density, and composition. Expanding the availability of laboratory measurements helps improve the reliability of disk models and provides deeper insights into the early stages of star and planet formation.

Acknowledgements. The authors appreciate the support of the Max-Planck Society. F.K. acknowledges support from the European Union's Horizon Europe research and innovation programme under the Marie Skłodowska-Curie Actions Postdoctoral Fellowship grant agreement No. # 101153804 (ORCHID). This project has also received funding from the European Union's Horizon 2020 research and innovation program under the Marie Skłodowska-Curie grant agreement # 811312 for the Project "Astro-Chemical Origins" (ACO). TPS and FTIR data processing and analysis by A.A.G., G.A.K., S.V.G., and K.I.Z. was supported by the RSF Project # 25–79–30006. D.C. acknowledges the Alexander von Humboldt Foundation for funding, as well as support from the University of Perugia with a postdoctoral research funding (assegno di ricerca), the AIAS–AUFF Fellowship Programme, funded by Aarhus University Research Foundation and Aarhus Institute of Advanced Studies (AIAS) at Aarhus University, and from the Danish National Research Foundation through the Center of Excellence "InterCat" (Grant agreement no.: DNRF150). The authors acknowledges the state of Baden-Württemberg through bwHPC and the German Research Foundation (DFG) through grant no INST 40/575-1 FUGG (JUSTUS 2 cluster).

References

Anderson, A. & Leroi, G. 1966a, The Journal of Chemical Physics, 45, 4359
 Anderson, A. & Leroi, G. E. 1966b, The Journal of Chemical Physics, 45, 4359
 Arabhavi, A. M., Woitke, P., Cazaux, S. M., et al. 2022, A&A, 666, A139
 Banks, P. A., Song, Z., & Ruggiero, M. T. 2020, Journal of Infrared, Millimeter, and Terahertz Waves, 41, 1411
 Becke, A. D. 1993, The Journal of Chemical Physics, 98, 5648
 Bergren, M. S., Schuh, D., Sceats, M. G., & Rice, S. A. 1978, J. Chem. Phys., 69, 3477
 Boogert, A. C. A., Gerakines, P. A., & Whittet, D. C. B. 2015, ARA&A, 53, 541
 Chen, Y., Liu, H., Deng, Y., et al. 2004, Chemical Physics Letters, 400, 357
 Cutini, M. & Ugliengo, P. 2021, The Journal of Chemical Physics, 155, 075102
 Dash, J., Ray, S., Nallappan, K., et al. 2015, The Journal of Physical Chemistry A, 119, 7991, pMID: 26114877
 Drążkowska, J. & Alibert, Y. 2017, A&A, 608, A92
 Gavdush, A., Ivlev, A., Zaytsev, K., et al. 2025, Astronomy & Astrophysics, under review
 Gavdush, A. A., Kruczakiewicz, F., Giuliano, B. M., et al. 2022, A&A, 667, A49
 Gavino, S., Kobus, J., Dutrey, A., et al. 2023, A&A, 680, A59
 Giuliano, B., Gavdush, A., Müller, B., et al. 2019, Astronomy & Astrophysics, 629, A112
 Griffiths, P. & de Haseth, J. 1986, Fourier transform infrared spectroscopy (New York, NY, USA: John Wiley & Sons)
 Grimme, S. 2006, Journal of Computational Chemistry, 27, 1787
 Gundlach, B. & Blum, J. 2015, ApJ, 798, 34
 Hagen, W. & Tielens, A. G. G. M. 1981, J. Chem. Phys., 75, 4198
 Hardy, J. R. & Karo, A. M. 1982, Physical Review B, 26, 3327
 Harris, F. 1978, Proceedings of the IEEE, 66, 51
 Hily-Blant, P., Walmsley, M., Pineau Des Forêts, G., & Flower, D. 2010, A&A, 513, A41
 Hudgins, D. M., Sandford, S. A., Allamandola, L. J., & Tielens, A. G. G. M. 1993, ApJS, 86, 713
 Jensen, F. 2014, J. Chem. Theory Comput., 10, 1074
 Kambara, O. 2014, in 2014 39th International Conference on Infrared, Millimeter, and Terahertz waves (IRMMW-THz), 1–2
 Kjems, J. K. & Dolling, G. 1975, Physical Review B, 11, 1639
 Kohin, B. C. 1960, The Journal of Chemical Physics, 33, 882
 Komandin, G., Zaytsev, K., Dolganova, I., et al. 2022, Optics Express, 30, 9208
 Lee, C., Yang, W., & Parr, R. G. 1988, Phys. Rev. B, 37, 785
 Louis, R. V. S. & Schnepp, O. 1969, The Journal of Chemical Physics, 50, 5177
 Lucas, J., Geron, E., Ditchi, T., & Hole, S. 2012, AIP Advances, 2, 032144
 Martin, P. 1967, Physical Review, 161, 143
 Minissale, M., Aikawa, Y., Bergin, E., et al. 2022, ACS Earth and Space Chemistry, 6, 597
 Müller, B., Giuliano, B. M., Bizzocchi, L., Vasyunin, A. I., & Caselli, P. 2018, A&A, 620, A46
 Neese, F. 2003, Journal of Computational Chemistry, 24, 1740

Table 2. Optically-active vibrational modes of the α -N₂ crystal found experimentally and calculated via DFT, as compared to some previous experimental and theoretical studies. Here, $k \equiv 1/\lambda = \nu/c_0$ stands for the spectroscopic wavenumber.

Method	ν_1 , THz (k_1 , cm ⁻¹)	ν_2 , THz (k_2 , cm ⁻¹)
Exp. (this work)	1.47 (49)	2.13 (71)
DFT (this work)	1.43 (47.57)	1.98 (66.07)
Exp. @ 10 K (Anderson & Leroi 1966b)	1.44 \pm 0.12 (48 \pm 4)	2.07 \pm 0.21 (69 \pm 7)
Exp. @ 15 K (Kjems & Dolling 1975)	1.45 \pm 0.02 (48.4 \pm 0.8)	2.08 \pm 0.05 (69.4 \pm 1.6)
Exp. @ 20 K (Ron & Schnepp 1967)	1.47 \pm 0.09 (49 \pm 3)	2.07 \pm 0.18 (69 \pm 6)
Int. potentials (Zunger & Huler 1975)	1.41 (47)	2.08 (69.5)

Neese, F. & Valeev, E. F. 2011, *J. Chem. Theory Comput.*, 7, 33
 Neese, F., Wennmohs, F., Becker, U., & Riplinger, C. 2020, *The Journal of Chemical Physics*, 152, 224108
 Öberg, K. I., Murray-Clay, R., & Bergin, E. A. 2011, *ApJ*, 743, L16
 Oppenheim, K. C., Korter, T. M., Melinger, J. S., & Grischkowsky, D. 2010, *The Journal of Physical Chemistry A*, 114, 12513, pMID: 21049898
 Qi, C., Öberg, K. I., Espaillat, C. C., et al. 2019, *The Astrophysical Journal*, 882, 160
 Ron, A. & Schnepp, O. 1967, *The Journal of Chemical Physics*, 46, 3991
 Savchenko, E., Khyzhniy, I., & Bondybey, V. 2019, *Low Temperature Physics*, 45, 975
 Scott, T. 1976, *Physics Reports*, 27, 89
 Stoychev, G. L., Auer, A. A., & Neese, F. 2017, *Journal of Chemical Theory and Computation*, 13, 554
 Sturm, J. A., McClure, M. K., Bergner, J. B., et al. 2023, *A&A*, 677, A18
 Tegler, S. C., Cornelison, D. M., Grundy, W. M., et al. 2010, *ApJ*, 725, 1296
 Tegler, S. C., Grundy, W. M., Olkin, C. B., et al. 2012, *ApJ*, 751, 76
 Tukey, J., Cleveland, W., & Brillinger, D. 1986, *The Collected Works of John W. Tukey*. Volume I: Time Series, 194–1964 (Wadsworth Statistics/Probability Series), 1st edn. (Wadsworth Advanced Books & Software)
 van 't Hoff, M. L. R., Walsh, C., Kama, M., Facchini, S., & van Dishoeck, E. F. 2017, *Astronomy & Astrophysics*, 599, A101
 Walsh, C., Millar, T. J., Nomura, H., et al. 2014, *A&A*, 563, A33
 Wang, Q. & Wang, H. 2012, *Chemical Physics Letters*, 534, 72
 Weigend, F. & Ahlrichs, R. 2005, *Phys. Chem. Chem. Phys.*, 7, 3297
 Wyckoff, R. 1963, *Crystal structures I* (book), Interscience Publishers, 1, 7
 Zunger, A. & Huler, E. 1975, *The Journal of Chemical Physics*, 62, 3010

Appendix A: DFT calculations

Table A.1 presents the far-infrared vibrational frequencies of the α -N₂ ice cluster model calculated using the B3LYP functional with different basis sets (Def2-SVP (Weigend & Ahlrichs 2005), pcseg-1 (Jensen 2014), ano-pvdz (Neese & Valeev 2011), and Def2-TZVP). The frequencies are shown both without (unrelaxed) and with (relaxed) optimization, except for the ano-pvdz basis set, which encountered convergence issues during optimization.

Without optimizing the structure, the Def2-TZVP basis set shows smaller deviations (1.43 and 4.93 cm⁻¹) with respect to the experimental values, while the pcseg-1 basis set shows the highest deviations (10.45 and 14.62 cm⁻¹). When adding the Grimme D3 dispersion correction (Grimme 2006), the frequencies exhibit a red shift of \simeq 4.66 cm⁻¹ for the lowest vibrational mode and \simeq 8.15 cm⁻¹ for the highest one.

When optimizing the experimental structure to a local minimum, the N₂ intramolecular distances vary depending on the basis set, while the intermolecular N–N distances do not deviate significantly. After optimization, we have noticed that the far-infrared spectrum completely changes, giving rise to infrared-active librations (oscillations along the center of mass of a diatomic molecule). This suggests that the far-infrared region is strongly sensitive to the N₂ interatomic distances. Hence, depending on the temperature, translational modes might vary or even disappear, giving rise to librational modes.

We expanded our cluster model by cutting it from a $3 \times 3 \times 3$ bulk of α -N₂ (Fig. A.1) and optimized it to evaluate the effect of size on reproducing the vibrational modes. Due to the large number of atoms, we were limited to using B3LYP/Def2-SVP due to computational constraints and only computed the partial Hessian numerically, making vibrational calculations only for the atoms within the $2 \times 2 \times 2$ box. Optimization using B3LYP-D3 leads to the appearance of librational modes, as the dispersion correction in this case underestimates intramolecular bond distances by \simeq 0.35 Å compared to B3LYP without dispersion.

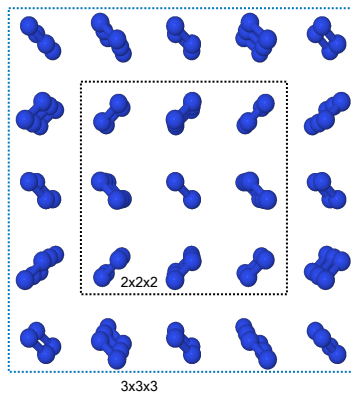


Fig. A.1. The balls and sticks model of the $3 \times 3 \times 3$ cluster of α -N₂ ice is derived by cutting a $3 \times 3 \times 3$ repeated bulk using the same procedure adopted for obtaining the $2 \times 2 \times 2$ cluster model, which is also schematically reported here for comparison.

Table A.1. DFT methods (Method) before optimization (unrelaxed) and after optimization (relaxed), vibrational frequencies (in the form of spectroscopic wavenumbers $k \equiv 1/\lambda = \nu/c_0$), intramolecular distances within a nitrogen molecule ($d(N-N)$), and intermolecular distances between two nitrogen molecules ($d(N₂-N₂)$) to simulate an α -N₂ cluster model. The computed frequencies for librational (L) and translational (not specified) modes are presented. Experimental values (Exp.) and theoretical results based on interatomic potentials (Int. potentials) are also reported.

Method	k, cm^{-1}	$d(N_2-N_2), \text{\AA}$	$d(N-N), \text{\AA}$
B3LYP/Def2-SVP (unrelaxed)	44.68, 63.97	3.64	1.05
B3LYP/pcseg-1 (unrelaxed)	38.55, 56.38	3.64	1.05
B3LYP/ano-pvdz (unrelaxed)	45.45, 64.06	3.64	1.05
B3LYP/Def2-TZVP (unrelaxed)	47.57, 66.07	3.64	1.05
B3LYP-D3/Def2-SVP (unrelaxed)	40.25, 55.83	3.64	1.05
B3LYP-D3/pcseg-1 (unrelaxed)	33.34, 48.13	3.64	1.05
B3LYP-D3/ano-pvdz (unrelaxed)	40.83, 55.77	3.64	1.05
B3LYP-D3/Def2-TZVP (unrelaxed)	43.18, 58.14	3.64	1.05
B3LYP/pcseg-1 (relaxed)	21(L), 28.89(L), 32.33(L), 35.58(L), 45.27(L)	3.81	1.1
B3LYP/Def2-TZVP (relaxed)	18.96, 30.49(L), 40.98(L)	4.07	1.09
B3LYP-D3/pcseg-1 (relaxed)	35.36(L), 45.63(L), 53.33(L), 53.84(L), 57.16(L), 60.42(L), 64.07(L)	3.46	1.1
B3LYP-D3/Def2-TZVP (relaxed)	24.3(L), 32.57(L), 49.95(L), 54.04(L), 64.22(L), 68.75(L)	3.61	1.09
B3LYP/Def2-SVP (relaxed)	27.41(L), 39.23(L), 39.72(L), 45.79(L), 47.09(L), 54.24(L)	3.75	1.1
B3LYP-D3/Def2-SVP (relaxed)	28.24(L), 36.71(L), 50(L), 60.49(L), 65.50(L), 68.95(L), 90.52(L), 106.84(L)	4.04	1.1
Exp. (this work)	49.0, 71 (@ 13 K)		
Exp. (Anderson & Leroi 1966b)	48 ± 4, 69 ± 7 (@ 10 K)		
Exp. (Kjems & Dolling 1975)	48.4 ± 0.8, 69.4 ± 1.6 (@ 15 K)		
Exp. (Ron & Schnepf 1967)	49 ± 3, 69 ± 6 (@ 20 K)		
Int. potentials (Kohin 1960)		4	1.1
Exp. (Kjems & Dolling 1975)		1.05	
Exp. (Kjems & Dolling 1975)		1.01	

*3x3x3 model.